Hot deformation characteristics of as-cast high-Cr ultra-super-critical rotor steel with columnar grains

Zong-ye Ding[1,2], *Qiao-dan Hu*[1,2], *Long Zeng*[1,2], *and Jian-guo Li*[1,2]

1) School of Materials Science and Engineering, Shanghai Jiao Tong University, Shanghai 200240, China

2) Laboratory of Advanced Materials and Solidification, Shanghai Jiao Tong University, Shanghai 200240, China

Abstract: Isothermal hot compression tests of as-cast high-Cr ultra-super-critical (USC) rotor steel with columnar grains perpendicular to the compression direction were carried out in the temperature range from 950 to 1250°C at strain rates ranging from 0.001 to 1 s^{-1}. The softening mechanism was dynamic recovery (DRV) at 950°C and the strain rate of 1 s^{-1}, whereas it was dynamic recrystallization (DRX) under the other conditions. A modified constitutive equation based on the Arrhenius model with strain compensation reasonably predicted the flow stress under various deformation conditions, and the activation energy was calculated to be 643.92 kJ·mol^{-1}. The critical stresses of dynamic recrystallization under different conditions were determined from the work-hardening rate (θ)–flow stress (σ) and $-\partial\theta/\partial\sigma$–$\sigma$ curves. The optimum processing parameters via analysis of the processing map and the softening mechanism were determined to be a deformation temperature range from 1100 to 1200°C and a strain-rate range from 0.001 to 0.08 s^{-1}, with a power dissipation efficiency η greater than 31%.

Keywords: rotor steel; columnar grains; dynamic recrystallization; constitutive models; critical conditions; processing maps

1. Introduction

Because of its excellent combination of high-temperature strength, high creep strength, and good resistance to environmental damage, high-Cr tempered martensite ferritic steel has often been used for ultra-super-critical (USC) rotor components in fossil-fuel-fired power plants [1–2]. The techniques used to manufacture high-Cr USC rotor steel, which include smelting, ingot casting, forging, and heat treatment, are important to its application [3]. Thus far, extensive attention has been devoted to the refining and casting technologies, heat treatment, creep resistance, and the fatigue properties of high-Cr steel, whereas the literature contains only a few reports related to its hot deformation behavior [4]. The addition of alloying element Cr should positively influence the corrosion and oxidation resistance of the steel, whereas Mo, W, V, and Nb should enhance its long-term creep strength via precipitation hardening. However, these various alloying elements adversely affect the deformation resistance of high-Cr USC rotor steel [5–6]. Thus, extensive efforts should be devoted to improving the

microstructures after deformation and processing efficiency of as-cast high-Cr USC rotor steel.

Equiaxed and columnar grains are well-known classical structures in castings and ingots of real materials, especially in plain carbon or low-alloy steel. Columnar structures are always observed in stainless steels and are difficult to eliminate completely during subsequent homogenization [7]. Investigations of the hot workability and processing parameters of various stainless steels with equiaxed grains under actual production conditions have been reported. Lü *et al.* [8] and Pu *et al.* [9] studied the hot deformation characteristics and optimized the processing parameters of super-austenitic stainless steels using constitutive equations and processing maps based on the dynamic materials model (DMM). Xi *et al.* [10] and Mirzadeh and Najafizadeh [11] investigated the critical conditions for dynamic recrystallization (DRX) of stainless steels on the basis of the inflection point of work hardening rate (θ)–flow stress (σ) and $-\partial\theta/\partial\sigma$–$\sigma$ curves. In the case of high-Cr steel with equiaxed structures, Wang *et al.* [12] calculated the Arrhenius constitutive equation at elevated temperatures and Wang *et al.* [13]

Springer

established processing maps to predict the process parameters of flow instability. However, no study on the hot deformation behavior, dynamic softening mechanisms, and hot working technology of as-cast high Cr USC rotor steel with columnar grains has yet been reported.

In this work, we carried out hot compression tests on as-cast high-Cr USC rotor steel with columnar grains at elevated temperatures and various strain rates; the compression direction was perpendicular to the columnar grains. On the basis of the experimental true stress–strain data, we established a modified constitutive equation with compensation of strain on materials constants and evaluated the reliability of the constitutive model. The critical conditions for DRX were calculated, and the microstructural evolution was

investigated. Further, the optimum processing parameters and the dynamic softening mechanisms under different conditions were analyzed.

2. Experimental

An ingot of high Cr USC rotor steel was fabricated under an argon atmosphere using an intermediate-frequency vacuum induction melting furnace. To obtain the columnar grains, the superheating temperature was set as 1700°C, the pouring temperature was 1600°C, and the liquid metal was cast in a sand mold preheated to 400°C (see Ref. [14] for details). The chemical composition of the as-cast high-Cr USC rotor steel is shown in Table 1.

Table 1. Chemical composition of the as-cast high-Cr USC rotor steel   wt%

Fe	Cr	Mo	V	W	Ni	Mn	Nb	C	N
86.34	10.50	1.06	0.18	0.98	0.75	0.45	0.055	0.12	0.052

The macrostructure of the ingot, the equilibrium phase constituents predicted using the JMatPro software, and a schematic of the deformed sample are shown in Fig. 1. Up to 85% of the area of the macrostructure is composed of columnar grains. The size (width) of the columnar grains in the center region is approximately 2 mm, whereas the columnar grains on the top and bottom are coarser. Cylinder specimens with a diameter of 10 mm and a height of 15 mm were machined from the position of the ingot instead of from the bottom negative segregation and hot top segregation zone, as shown in Fig. 1(a). The size of the columnar grains in the

deformed samples is approximately 2 mm. A schematic diagram of a deformed sample with the compression direction perpendicular to the columnar grains is shown in Fig. 1(c). To retain the lubricant composed of graphite mixed with machine oil during the hot compression tests, convex depressions with a depth of 0.2 mm were machined on both ends of the samples. The equilibrium phase diagram for the chemical compositions of the sample was calculated using the JMatPro software, as shown in Fig. 1(b). The samples with austenite should form in the temperature range from 900 to 1300°C, where DRX tends to occur [15].
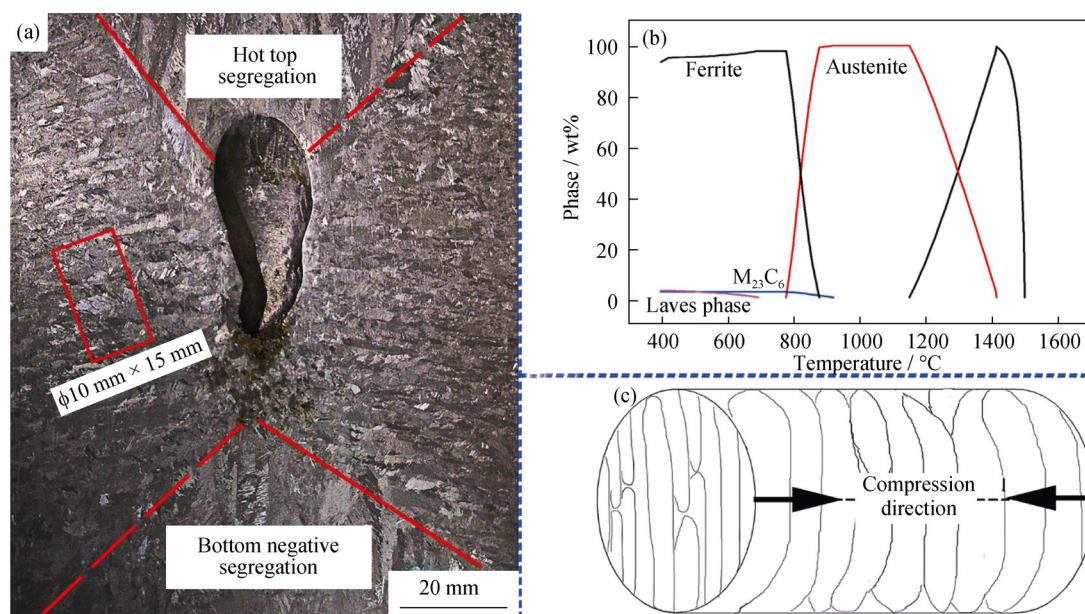

Fig. 1. (a) Macrostructure of the as-cast high-Cr USC steel ingot; (b) phase diagram calculated using the JMatPro software; (c) schematic of a deformed sample.

The thermophysical simulation experiments were performed on a Gleeble-3500 machine at temperatures of 950, 1050, 1150, and 1250°C and at strain rates of 0.001, 0.01, 0.1, and 1 s^{-1}; the total deformation amount was 0.8. To ensure a uniform temperature, the samples were heated to the deformation temperature at 5°C·s^{-1} and maintained at this temperature for 2 min prior to deformation. After the compression tests, the samples were water quenched to room temperature to retain the hot deformation microstructures. The samples were mechanically polished and then etched with a solution of K_2MnO_4 (2.5 g) + H_2O (10 mL) + H_2SO_4 (90 mL) at 75°C. The microstructures were observed by optical microscopy.

3. Results and discussion

3.1. Flow stress behavior and microstructural characterization

The flow stress (σ)–strain (ε) curves of the as-cast high-Cr USC rotor steel with columnar grains under different conditions are shown in Fig. 2. At a strain rate of 1 s^{-1} and different temperatures, the flow stress increases until reaching a peak value, then attains a steady state, exhibiting typical dynamic recovery (DRV) behavior [16]. At a temperature of 950°C, the flow stress shows a sharp increase to a peak stress and enters steady-state flow, as shown in Fig. 2(a). Large-scale deformation bands, broken delta ferrites, and cracks are clearly observed in the deformed sample (Fig. 3(a)), consistent with the flow stress behavior. Similar behavior has been reported during hot deformation of 00Cr23Ni4N duplex stainless steel [17]. The flow stress behavior indicates an interaction between the work-hardening and DRV mechanisms. At a strain rate of 1 s^{-1} and temperatures greater than 1050°C, the flow stress increases gradually to a peak value and then attains a steady state (Figs. 2(b)–2(d)). The curve of the sample at 950°C and 0.1 s^{-1} is abnormal; this test was repeated several times, and the abnormal results will be investigated in future work. New equiaxed grains are observed, which indicates the occurrence of DRX, as shown in Figs. 3(d) and 3(g). At 1050°C (Fig. 3(d)), necklace structures are observed along the columnar grain boundaries, which is a typical structure developed during discontinuous dynamic recrystallization (DDRX) [18].
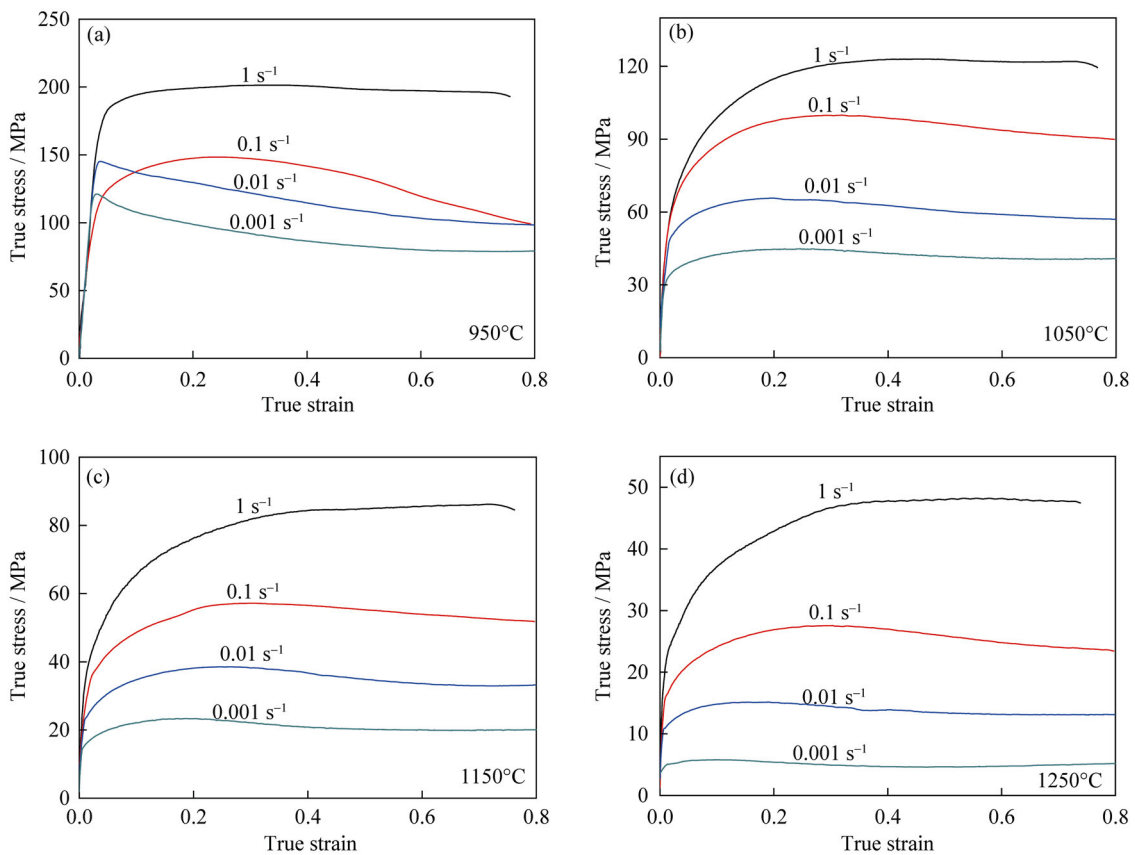

Fig. 2.   Flow curves of samples deformed at different temperatures and strain rates: (a) 950°C; (b) 1050°C; (c) 1150°C; (d) 1250°C.
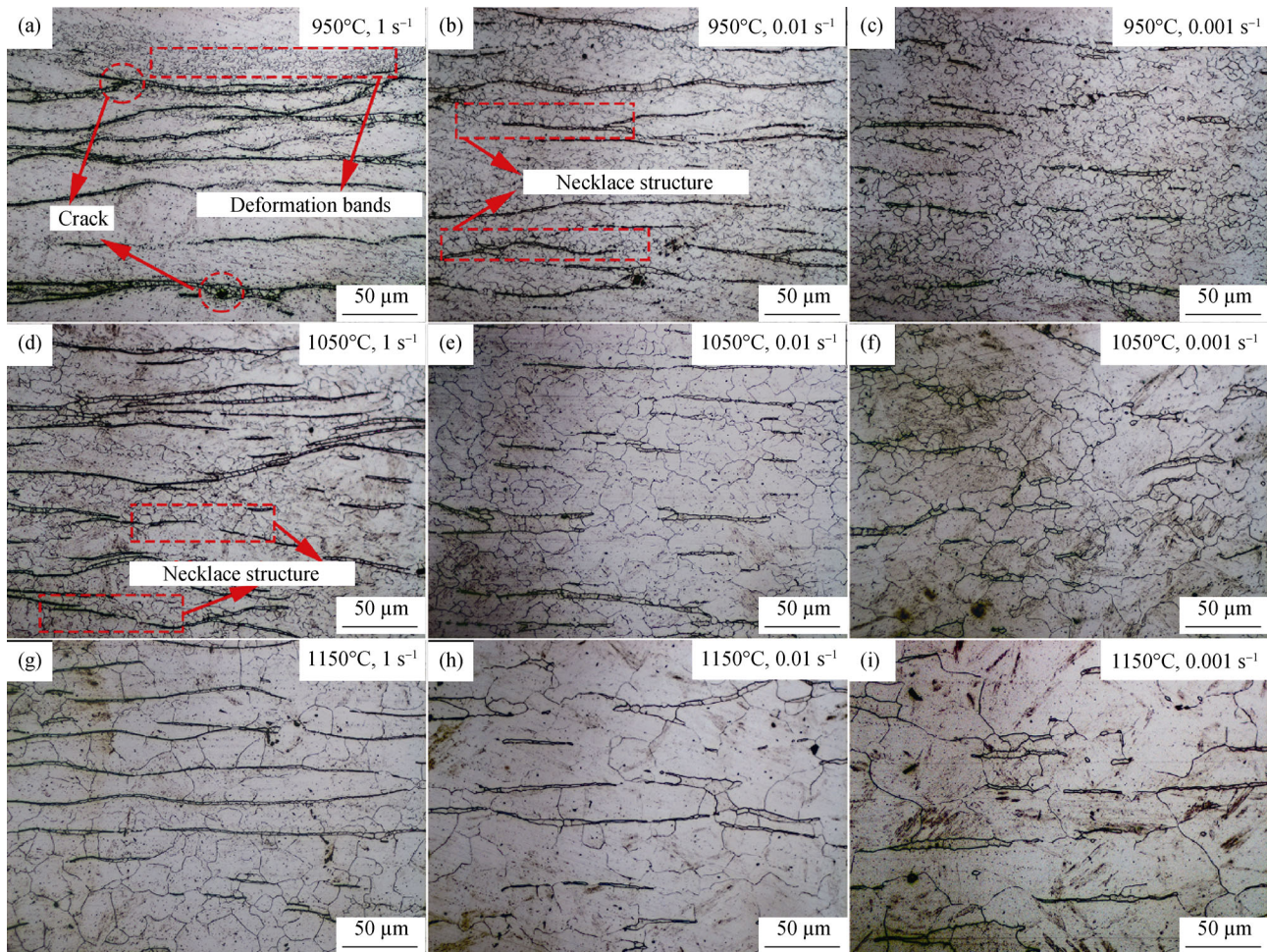
Fig. 3. Microstructures of the high-Cr steel under different deformation conditions and a strain of 0.8: (a) 950°C, 1 s⁻¹; (b) 950°C, 0.01 s⁻¹; (c) 950°C, 0.001 s⁻¹; (d) 1050°C, 1 s⁻¹; (e) 1050°C, 0.01 s⁻¹; (f) 1050°C, 0.001 s⁻¹; (g) 1150°C, 1 s⁻¹; (h) 1150°C, 0.01 s⁻¹; (i) 1150°C, 0.001 s⁻¹.

At strain rates from 0.001 to 0.1 s⁻¹ and various temperatures, the flow stress reaches a peak at a certain strain and then decreases to a steady state, as illustrated in Figs. 2(b)–2(d). Figs. 3(b)–3(i) show that DRX grains were formed in the deformed samples. The flow stress behavior can be explained on the basis of the dynamic balance between work hardening and DRX.

Fig. 2 shows that the flow stress decreases with increasing deformation temperature, which is attributed to enhancement of DRV, dislocation motion and grain-boundary diffusion, and the decrease of grain-boundary shear resistance at high temperatures. In addition, the flow stress increases with increasing strain rate, which is ascribed to the impediment of local dislocation tangles from dislocation accumulation [19]. Obviously, the peak stress σ_p and peak strain ε_p decrease with increasing deformation temperature or decreasing strain rate. At a strain rate of 0.01 s⁻¹ and deformation temperatures from 950 to 1150°C, the DRX grains grow with increasing deformation temperature (Figs.

3(b), 3(e), and 3(h)). The columnar grains were completely replaced by DRX grains at 1050°C. At 950°C and strain rates from 0.001 to 1 s⁻¹, DRX grains appear and increase in number with decreasing strain rate, as shown in Figs. 3(a)–3(c). As the temperature is further increased to 1150°C, larger DRX grains are formed with decreasing strain rate (Figs. 3(g)–3(i)). At higher temperatures and lower strain rates, more movable dislocations and multiple slip systems are present in the high-Cr USC rotor steel, which can result in lower stresses and more or larger equiaxed grains. This observation is consistent with the analysis of the flow stress behavior of other steels with equiaxed grains [20–21].

The fraction and size of DRX grains increase with increasing temperature or decreasing strain rate. The deformation conditions, such as temperature, strain rate, and strain, strongly influence the flow stress behavior and microstructures of the as-cast high-Cr USC rotor steel with columnar grains. The relationship between flow stress and deformation parameters can be expressed by a constitutive model.

3.2. Constitutive relation and verification

The relationship among the flow stress (σ), deformation temperature (T), and the strain rate ($\dot{\varepsilon}$) is expressed by the classical hyperbolic sine function, and the Zener–Hollomon parameter (Z) is introduced [22–23]:

$$\ln\dot{\varepsilon} = \ln A - Q/RT + n\ln\sigma \text{ , } \alpha\sigma < 0.8 \quad (1)$$

$$\ln\dot{\varepsilon} = \ln A - Q/RT + \beta\sigma \text{ , } \alpha\sigma > 1.2 \quad (2)$$

$$\ln\dot{\varepsilon} = \ln A + n\ln[\sinh(\alpha\sigma)] - Q/RT \text{ , for all } \alpha\sigma \quad (3)$$

$$Z = \dot{\varepsilon}\exp(-Q/RT) \quad (4)$$

where A and β are material constants, Q is the activation energy (J·mol^{-1}), R is the gas constant ($R = 8.314$ J·mol^{-1}·K^{-1}),

and T is the deformation temperature (K). The value of n ($n = 5.05$) and β ($\beta = 0.093$) can be obtained from the relative curves of flow stress and strain rate shown in Figs. 4(a) and 4(b). Because $\alpha = \beta/n$, the value of α was calculated as 0.01841. From the $\ln[\sinh(\alpha\sigma)] - \ln\dot{\varepsilon}$ plots and the $\ln[\sinh(\alpha\sigma)] - 1000/T$ plots (Figs. 4(c) and 4(d)), the activation energy Q was calculated as 643.92 kJ·mol^{-1}, which is larger than the value for the high-Cr steel with equiaxed grains calculated by Wang *et al.* [13]. Compared to the samples with equiaxed grains after homogenization, the as-cast samples with columnar grains exhibit less consistent grain boundaries, fewer slip bands, and a higher level of composition
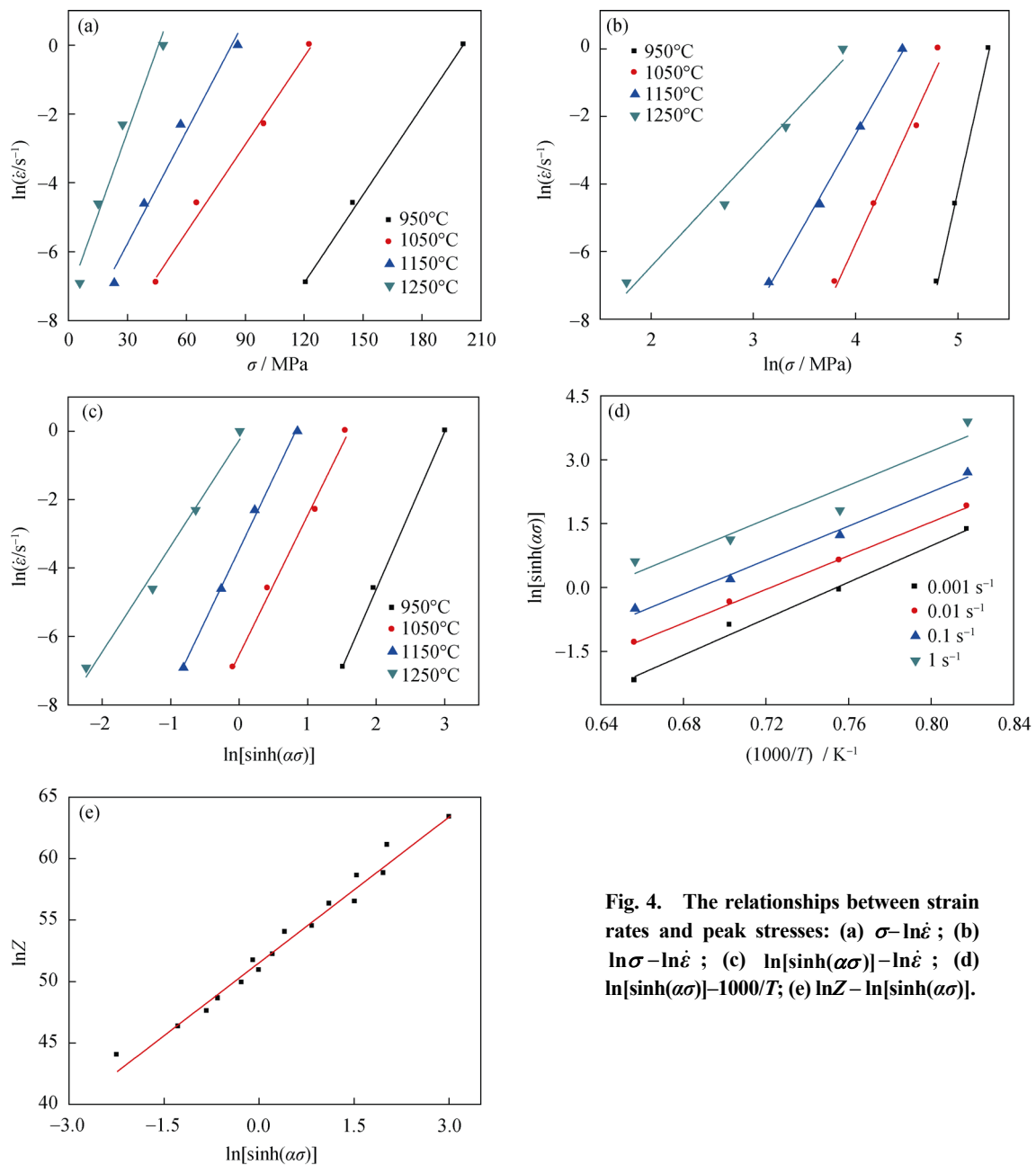

Fig. 4.   The relationships between strain rates and peak stresses: (a) $\sigma - \ln\dot{\varepsilon}$; (b) $\ln\sigma - \ln\dot{\varepsilon}$; (c) $\ln[\sinh(\alpha\sigma)] - \ln\dot{\varepsilon}$; (d) $\ln[\sinh(\alpha\sigma)] - 1000/T$; (e) $\ln Z - \ln[\sinh(\alpha\sigma)]$.

segregation; all of these factors make deformation more difficult. According to the $\ln[\sinh(\alpha\sigma)]$–$\ln Z$ curve (Fig. 4(e)), the hot deformation constitutive equation of the as-cast high-Cr USC rotor steel with a columnar structure was determined as

$$\dot{\varepsilon} = e^{51.52}[\sinh(0.0184\sigma)]^{3.956}\exp(-643920/8.314T) \quad (5)$$

Given the effect of strain on the deformation behavior, the Arrhenius-type constitutive model should be modified by compensation of strain. In this paper, we calculated the α, n, A, and Q values with various strains at an interval of 0.025 and fitted these material parameters versus strain using a fifth-order polynomial (Eq. (6)):

$$\begin{cases} \alpha = B_0 + B_1\varepsilon + B_2\varepsilon^2 + B_3\varepsilon^3 + B_4\varepsilon^4 + B_5\varepsilon^5 \\ Q = C_0 + C_1\varepsilon + C_2\varepsilon^2 + C_3\varepsilon^3 + C_4\varepsilon^4 + C_5\varepsilon^5 \\ \ln A = D_0 + D_1\varepsilon + D_2\varepsilon^2 + D_3\varepsilon^3 + D_4\varepsilon^4 + D_5\varepsilon^5 \\ n = E_0 + E_1\varepsilon + E_2\varepsilon^2 + E_3\varepsilon^3 + E_4\varepsilon^4 + E_5\varepsilon^5 \end{cases} \quad (6)$$

The fitting curves are shown in Fig. 5, and the relevant constants calculated from the curves are shown in Table 2. The results indicate that a fifth-order polynomial fits the relationship between the material parameters and strains with a very good correlation ($R^2 > 0.993$).

To verify the accuracy of the developed constitutive model with the compensation of strain, we calculated the predicted flow stresses under different deformation conditions at strains ranging from 0.05 to 0.7 in intervals of 0.025 using Eq. (7):

$$\sigma = \ln\left\{(Z/A)^{1/n} + \left[(Z/A)^{2/n} + 1\right]^{1/2}\right\}\Big/\alpha \quad (7)$$

A comparison between the predicted and experimental values is shown in Fig. 6, which reveals that the predicted and experimental values are closely correlated. To further verify the accuracy of the compensated constitutive equation, we calculated the correlation coefficient (R), the root-mean-square error (RSME), and the average absolute relative error (AARE) using Eq. (8):

$$\begin{cases} R = \sum_{i=1}^{N}\left(E_i - \overline{E}\right)\left(P_i - \overline{P}\right)\Big/\sqrt{\sum_{i=1}^{N}\left(E_i - \overline{E}\right)^2\left(P_i - \overline{P}\right)^2} \\ \text{RMSE} = \sqrt{\sum_{i=1}^{N}\left(E_i - P_i\right)^2\Big/N} \\ \text{AARE}(\%) = \sum_{i=1}^{N}\left|\left(E_i - P_i\right)/E_i\right|\times100\Big/N \end{cases} \quad (8)$$

where N is the total number of data points, E_i is the experimental stress, P_i is the calculated stress, and $\overline{E}$ and $\overline{P}$ are the mean values of E_i and P_i, respectively.
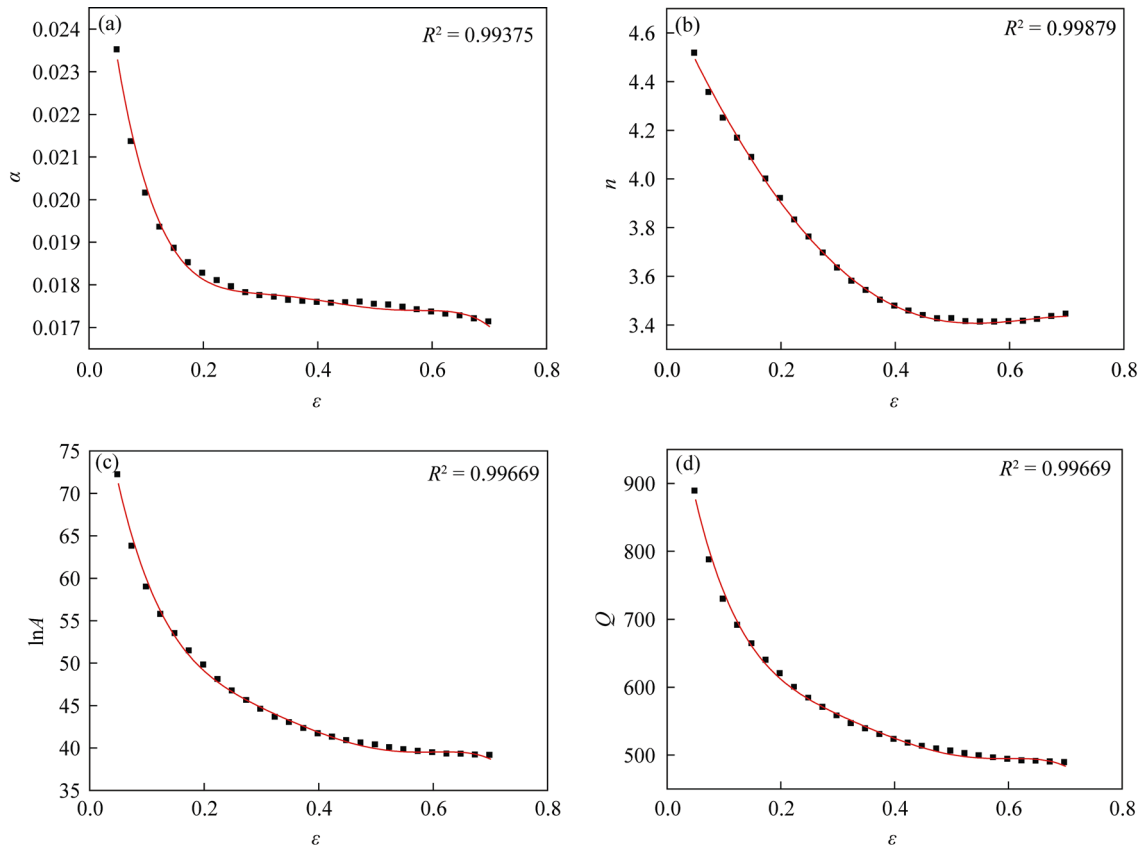
Fig. 5.   Curves of α, n, A, and Q versus strain: (a) α–ε; (b) n–ε; (c) A–ε; and (d) Q–ε.

Table 2.   Coefficients of polynomial of as-cast high Cr USC rotor steel for *α*, *n*, *A*, and *Q*

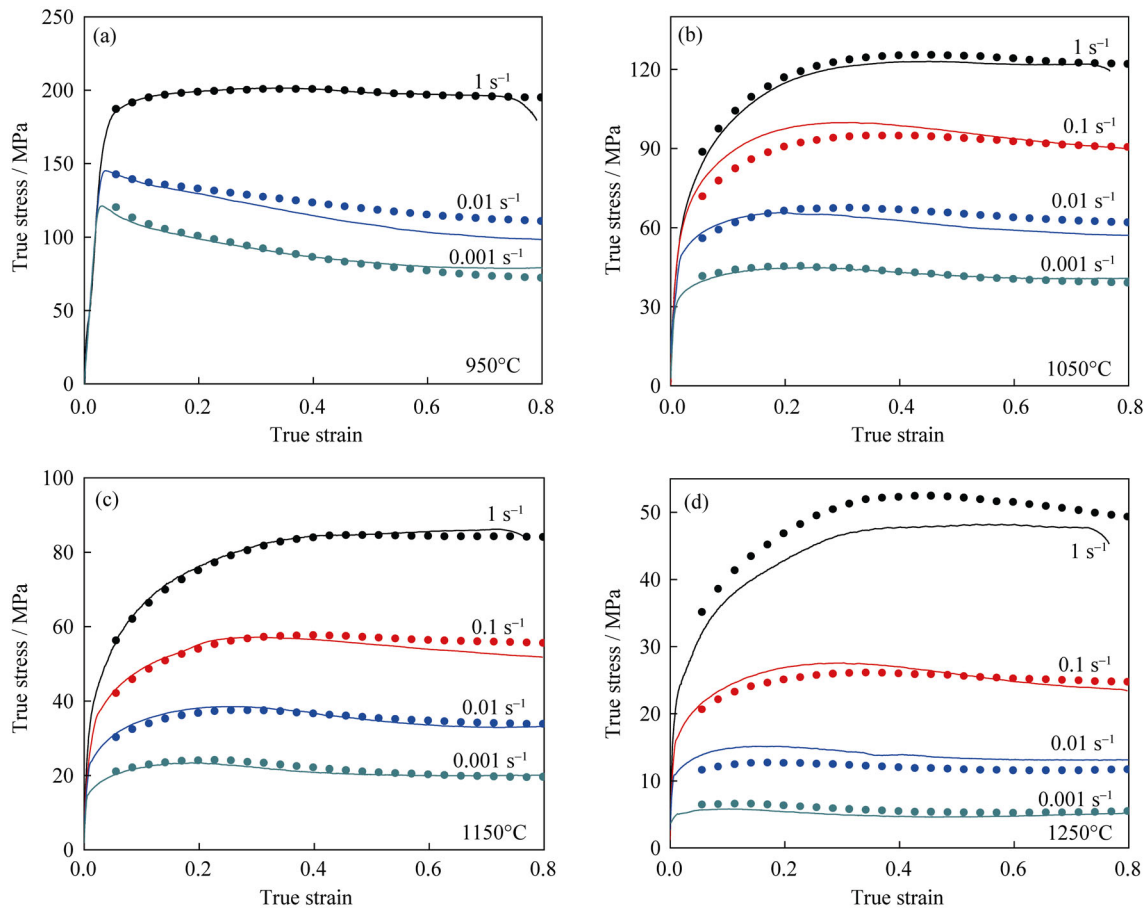| α	Q	lnA	n
$B_0 = 0.0285$	$C_0 = 1099.99599$	$D_0 = 89.71071$	$E_0 = 4.73183$
$B_1 = -0.1341$	$C_1 = -5626.33408$	$D_1 = -465.95609$	$E_1 = -5.05594$
$B_2 = 0.66523$	$C_2 = 25751.44791$	$D_2 = 2121.13575$	$E_2 = 4.21167$
$B_3 = -1.61697$	$C_3 = -62942.39829$	$D_3 = -5167.07345$	$E_3 = 1.52156$
$B_4 = 1.90249$	$C_4 = 76048.44879$	$D_4 = 6235.57979$	$E_4 = 1.61512$
$B_5 = -0.86715$	$C_5 = -35496.93986$	$D_5 = -2909.7525$	$E_5 = -4.34303$

Fig. 6.   Comparison between predicted and experimental flow stresses under different conditions: (a) 950°C; (b) 1050°C; (c) 1150°C; and (d) 1250°C.

The comprehensive correlations between calculated and experimental values and the error distribution are illustrated in Fig. 7. From Fig. 7(a), the value of *R* is 0.9984, which indicates a good linear relationship between calculated and experimental flow stresses but cannot verify the accuracy of the constitutive equation. The RSME and AARE values, which are unbiased statistical parameters, were calculated to be as low as 2.845 MPa and 4.637%, respectively. As shown in Fig. 7(b), most of errors are in the range from −2.5 to 2.5 and the frequency of error fol-

lows a Gaussian distribution. The mean ($\bar{\mu}$) and standard deviation (*r*) for the as-cast high-Cr USC rotor steel are 0.3067 and 6.572, respectively. In general, the compensated Arrhenius-type constitutive equation accurately describes the flow stresses of the as-cast high-Cr USC rotor steel with columnar grains.

3.3. Critical conditions of DRX

According to the approaches of Poliak and Jonas [24] and Ryan and McQueen [25], the critical stresses for ini-

tiation of DRX can be determined from the inflection points in the θ–σ plots or from the minima in the $-\partial\theta/\partial\sigma$–$\sigma$ curves. Figs. 8(a)–8(c) display the work-hardening-rate curves of the as-cast high-Cr USC rotor steel with columnar grains under various deformation conditions. The θ decreases abruptly at the initial stage of DRX, which is attributed to an increase in dislocation density. Subsequently, the θ gradually decreases to inflection points and finally reaches zero with the softening of DRX, which indicates that the flow stress is the peak value. The relationship between θ and σ was fitted using a third-order polynomial equation [26]:

$$\theta = A_1\sigma^3 + A_2\sigma^2 + A_3\sigma + A_4 \tag{9}$$

where A_1, A_2, A_3, and A_4 are constants for a given set of deformation conditions. Because $\partial^2\theta/\partial^2\sigma$ equals zero, the critical stress for initiation of DRX can be expressed as

$$\partial^2\theta/\partial^2\sigma = 0 \Rightarrow \sigma_c = -A_2/3A_1 \tag{10}$$

The curves of $-\partial\theta/\partial\sigma$ versus σ are shown in Figs. 8(d)–8(f). Minimum points are observed in the $-\partial\theta/\partial\sigma$–$\sigma$ curves; these points represent the critical stresses under various deformation conditions. In addition, the critical stress decreases with increasing deformation temperature or decreasing strain rate, which indicates that the occurrence of DRX would be easier at higher temperatures or lower strain rates, consistent with the results reported by Han *et al.* [27].
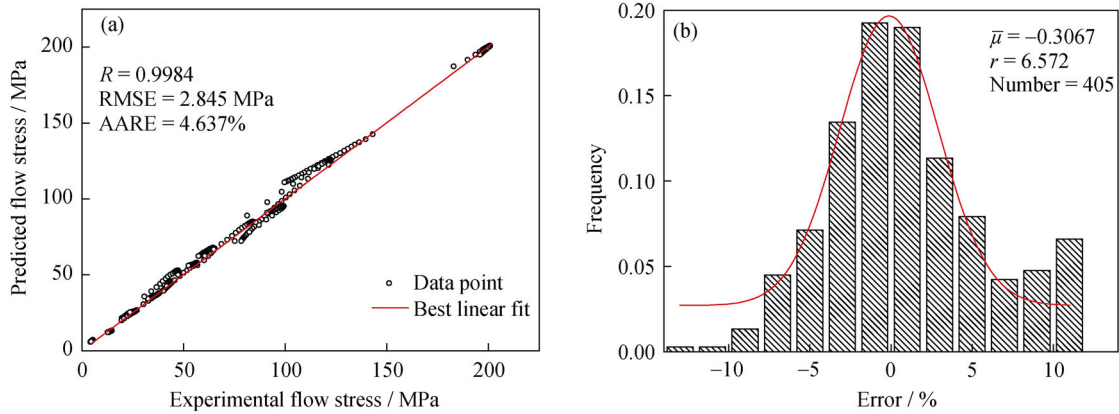

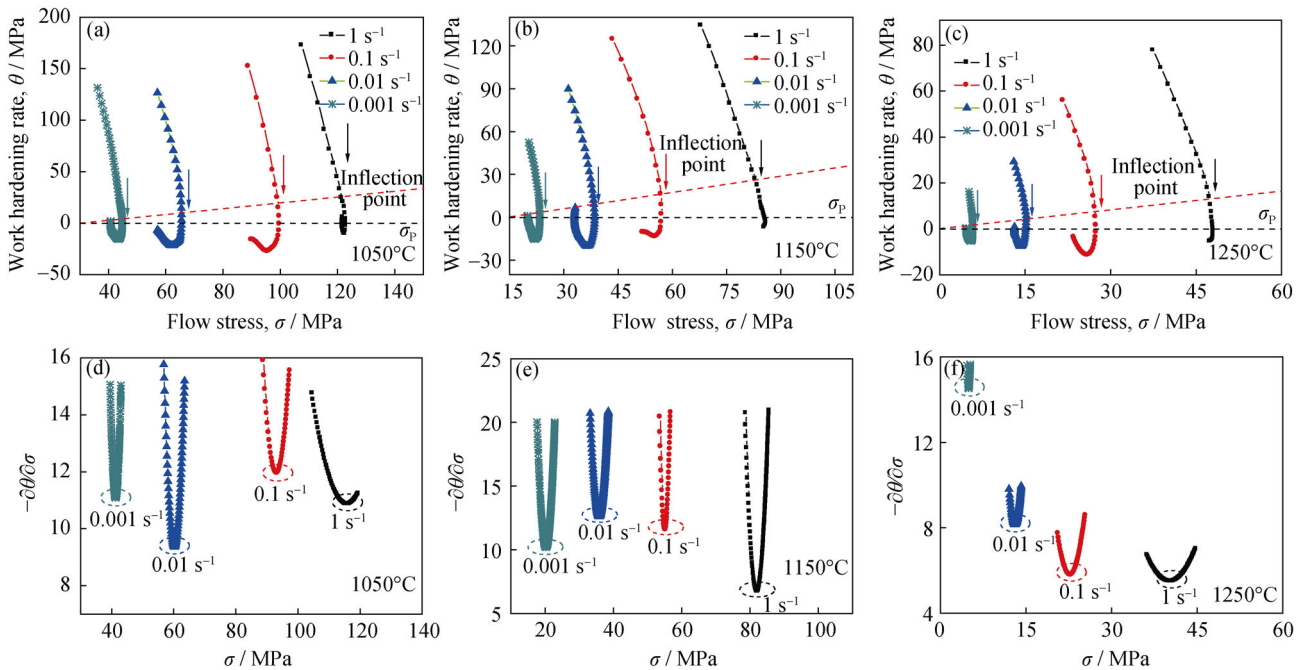Fig. 7.   (a) Correlation between predicted and experimental flow stresses; (b) error distribution.

Fig. 8. θ–σ curves: (a) 1050°C, (b) 1150°C, and (c) 1250°C; $-\partial\theta/\partial\sigma$–$\sigma$ curves: (d)1050°C, (e)1150°C, and (f)1250°C.

Fig. 9 shows the optical micrographs of the samples deformed at 1050°C, the strain rate 0.01 s^{-1}, and various strains. δ-Ferrite is observed between lath martensites in the as-cast sample, as shown in Fig. 9(a). At a strain of 0.15, the δ-ferrite is broken and the DRX grain appears adjacent to the δ-ferrite (Fig. 9(b)). The stress at the strain of 0.15 is larger than the critical stress obtained from Eq. (10). The occurrence of DRX confirms the analysis of the critical conditions of DRX for the as-cast high-Cr USC rotor steel with columnar grains. With increasing strain, more DRX grains would be formed. At a strain of 0.8, the columnar grains were completely replaced by the DRX grains (Figs. 9(c) and 9(d)).
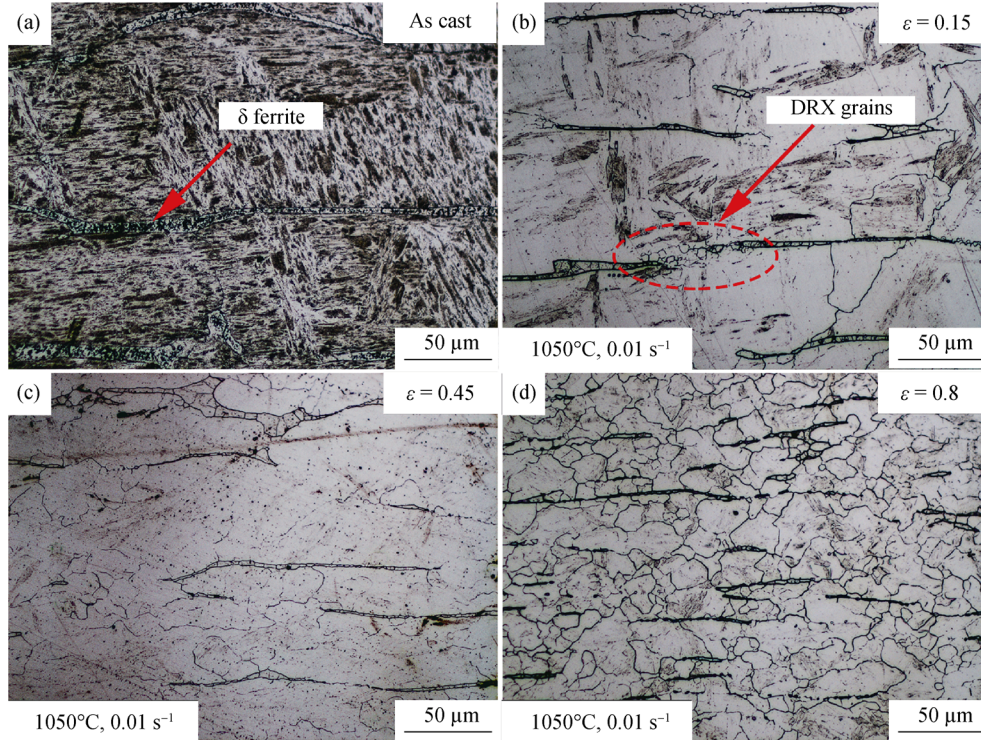

Fig. 9.   Microstructures of the high-Cr USC rotor steel at 1050°C and 0.01 s^{-1} with different strains.

3.4. Application of processing map

On the basis of the dynamic material model (DMM), the processing map can be obtained by superimposing an instability map over a power dissipation map. To evaluate the power dissipation during microstructural evolution, the efficiency of power dissipation (η) is calculated by [28]

$$\eta = 2m/(m+1) \tag{11}$$

where m is a strain-rate sensitivity parameter. To identify the regime of flow instability, the instability criterion is expressed by [29]

$$\xi(\dot{\varepsilon}) = \partial \ln\left[m/(m+1)\right]/\partial \ln \dot{\varepsilon} + m < 0 \tag{12}$$

where $\xi(\dot{\varepsilon})$ is a dimensionless instability parameter. The negative instability parameter ξ represents the material being located in the flow instability region. Fig. 10(a) shows the processing map for the as-cast high-Cr USC rotor steel with columnar grains in the temperature range from 950 to 1250°C and for the strain-rate range from 0.001 to 1 s^{-1} at a strain of 0.6. The counter-plot values indicate the percent efficiency of power dissipation, and the white and gray regions represent flow stability and flow instability areas, respectively. Fig. 10(a) shows that the power dissipation efficiency values increase with increasing deformation temperature. The high value of η corresponds to the occurrence of DRX [15]. Two instability regions are observed in the regions with low temperatures and/or high strain rates; these regions should be avoided during processing.

A schematic of the microstructure evolution mechanism of the as-cast high-Cr USC rotor steel with columnar grains during hot compression deformation was constructed on the basis of the flow stress, microstructures, and processing map, as shown in Fig. 10(b). The DRV, partial DRX, DRX, grain-growth, and instability regions are displayed. Generally, the microstructure preferred in the hot working process is characterized by fine and equiaxed DRX grains, which results in high power dissipation efficiency, stable flow, and good workability [30]. Consequently, the optimum hot working parameters are obtained in the deformation temperature range from 1100 to 1200°C and in the strain-rate range from 0.001 to 0.08 s^{-1}, with a power dissipation efficiency $\eta > 31\%$.
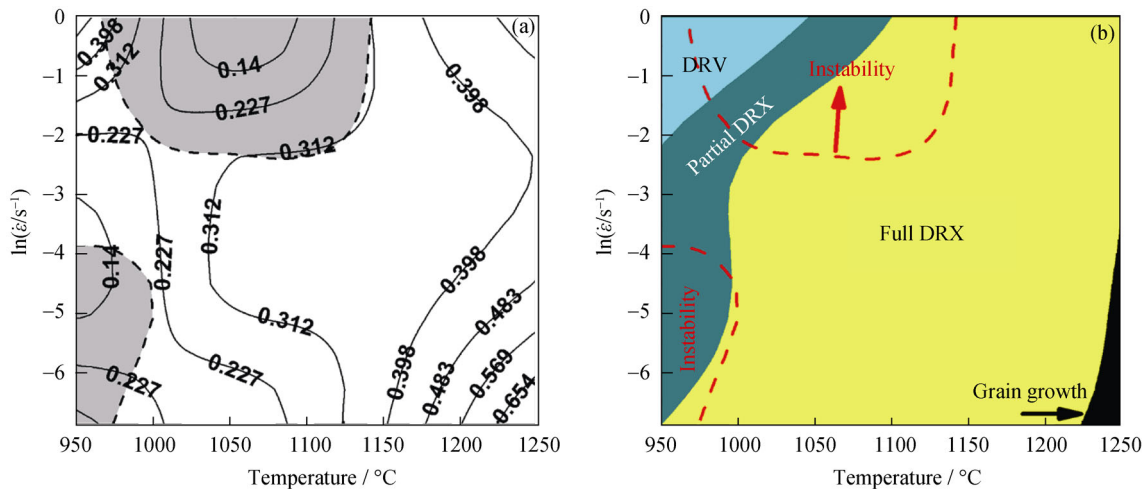
Fig. 10. (a) Processing map for the as-cast high-Cr USC rotor steel with columnar grains at a strain of 0.6; (b) schematic of the microstructure evolution mechanism of the steel during hot deformation.

4. Conclusions

The hot deformation behavior of as-cast high-Cr USC rotor steel with compression direction perpendicular to columnar grains was investigated. The flow stress behavior and microstructures of specimens deformed under various conditions were studied, and a constitutive equation with compensation of strain was deduced and verified. The critical conditions of DRX were determined, and the optimum processing window for the material was obtained. We drew the following conclusions:

(1) The flow stress and microstructural evolution are dependent on the deformation temperature, strain rate, and strain. The softening mechanism is DRV at 950°C and 1 s^{-1}, whereas it is DRX under other conditions.

(2) The modified Arrhenius-type constitutive equation with the compensation of strain reasonably predicts the flow stresses at different temperatures and various strain rates. The comprehensive correlations and error distribution between the predicted and experimental values were analyzed.

(3) The critical stresses of DRX under various deformation conditions are determined from the θ–σ and $-\partial\theta/\partial\sigma$–$\sigma$ curves.

(4) The optimum hot working conditions are obtained in the temperature range from 1100 to 1200°C and the strain rate range from 0.001 to 0.08 s^{-1}.

Acknowledgements

References

[1] M.I. Isik, A. Kostka, V.A. Yardley, K.G. Pradeep, M.J. Duarte, P.P. Choi, D. Raabe and G. Eggeler, The nucleation of Mo-rich Laves phase particles adjacent to $M_{23}C_6$ micrograin boundary carbides in 12% Cr tempered martensite ferritic steels, *Acta Mater.*, 90(2015), p. 94.

[2] G. Götz and W. Blum, Influence of thermal history on precipitation of hardening phases in tempered martensite 10%Cr-steel X12CrMoWVNbN 10-1-1, *Mater. Sci. Eng. A*, 348(2003), No. 1-2, p. 201.

[3] F. Chen, Z.S. Cui, D.S. Sui, and B. Fu, Recrystallization of 30Cr2Ni4MoV ultra-super-critical rotor steel during hot deformation: Part III. Metadynamic recrystallization, *Mater. Sci. Eng. A*, 540(2012), p. 46.

[4] F. Chen, Z.S. Cui, and S.J. Chen, Recrystallization of 30Cr2Ni4MoV ultra-super-critical rotor steel during hot deformation: Part I. Dynamic recrystallization, *Mater. Sci. Eng. A*, 528(2011), No. 15, p. 5073.

[5] J. Hald, Microstructure and long-term creep properties of 9-12% Cr steels, *Int. J. Pressure Vessels Piping*, 85(2008), No. 1-2, p. 30.

[6] R.L. Klueh and A.T. Nelson, Ferritic/ martensitic steels for next-generation reactors, *J. Nucl. Mater.*, 371(2007), No. 1-3, p. 37.

[7] M.C. Flemings, Solidification processing, *Metall. Trans.*, 5(1974), p. 2121.

[8] G.W. Liu, Y. Han, Z.Q. Shi, J.P. Sun, D.N. Zou, and G.J.

Qiao, Hot deformation and optimization of process parameters of an as-cast 6Mo superaustenitic stainless steel: a study with processing map, *Mater. Des.*, 53(2014), p. 662.

[9] E.X. Pu, W.J. Zheng, J.Z. Xiang, Z.G. Song, and J. Li, Hot deformation characteristic and processing map of superaustenitic stainless steel S32654, *Mater. Sci. Eng. A*, 598(2014), p. 174.

[10] T. Xi, C.G. Yang, M. Babar Shahzad, and K. Yang, Study of the processing map and hot deformation behavior of a Cu-bearing 317LN austenitic stainless steel, *Mater. Des.*, 87(2015), p. 303.

[11] H. Mirzadeh and A. Najafizadeh, Hot deformation and dynamic recrystallization of 17-4 PH stainless steel, *ISIJ Int.*, 53(2013), No. 4, p. 680.

[12] B.Z. Wang, W.T. Fu, Z.Q. Lv, P. Jiang, W.H. Zhang, and Y.J. Tian, Study on the hot deformation behavior of 12%Cr ultra-super-critical rotor steel, *Mater. Sci. Eng. A*, 487(2008), No. 1-2, p. 108.

[13] Z.H. Wang, W.T. Fu, B.Z. Wang, W.H. Zhang, Z.Q. Lv, and P. Jiang, Study on hot deformation characteristics of 12%Cr ultra-super-critical rotor steel using processing maps and Zener−Hollomon parameter, *Mater. Charact.*, 61(2010), No. 1, p. 25.

[14] L. Zeng, M.Q. Xu, X.R. Ma, Y.J. Huang, S.G. Zhang, Q.D. Hu, and J.G. Li, Grain refinement and delta ferrite reduction of high Cr steel ingots by thermal control, *ISIJ Int.*, 54(2014), No. 10, p. 2302.

[15] C. Zhang, L.W. Zhang, W.F. Shen, C.R. Liu, Y.N. Xia, and R.Q. Li, Study on constitutive modeling and processing maps for hot deformation of medium carbon Cr−Ni−Mo alloyed steel, *Mater. Des.*, 90(2016), p. 804.

[16] Z.Y. Ding, S.G. Jia, P.F. Zhao, M. Deng, and K.X. Song, Hot deformation behavior of Cu−0.6Cr−0.03Zr alloy during compression at elevated temperatures, *Mater. Sci. Eng. A*, 570(2013), p. 87.

[17] Y. Han, D.N. Zou, Z.Y. Chen, G.W. Fan, and W. Zhang, Investigation on hot deformation behavior of 00Cr23Ni4N duplex stainless steel under medium-high strain rates, *Mater. Charact.*, 62(2011), No. 2, p. 198.

[18] D. Ponge and G. Gottstein, Necklace formation during dynamic recrystallization: mechanisms and impact on flow behavior, *Acta Mater.*, 46(1998), No. 1, p. 69.

[19] J. Luo, L.F. Wang, S.F. Liu, and M.Q. Li, The correlation between the flow behavior and the microstructure evolution during hot working of TC18 alloy, *Mater. Sci. Eng. A*, 654(2016), p. 213.

[20] H. Farnoush, A. Momeni, K. Dehghani, J. Aghazadeh Mohandesi, and H. Keshmiri, Hot deformation characteristics of 2205 duplex stainless steel based on the behavior of constituent phases, *Mater. Des.*, 31(2010), No. 1, p. 220.

[21] G.R. Ebrahimi, H. Keshmiri, A.R. Maldar, and A. Momeni, Dynamic recrystallization behavior of 13%Cr martensitic stainless steel under hot working condition, *J. Mater. Sci. Technol.,* 28(2012), No. 5, p. 467.

[22] C.M. Sellars and W.J. McG. Tegart, Hot workability, *Int. Metall. Rev.*, 17(1972), No. 1, p. 1.

[23] J. Wang, G.Q. Zhao, L. Chen, and J.L. Li, A comparative study of several constitutive models for powder metallurgy tungsten at elevated temperature, *Mater. Des.*, 90(2016), p. 91.

[24] E.I. Poliak and J.J. Jonas, A one-parameter approach to determining the critical conditions for the initiation of dynamic recrystallization, *Acta Mater.*, 44(1996), No. 1, p. 127.

[25] N.D. Ryan and H.J. McQueen, Dynamic softening mechanisms in 304 austenitic stainless steel, *Can. Metall. Q*, 29(1990), No. 2, p. 147.

[26] D.Q. Dong, F. Chen, and Z.S. Cui, A physically-based constitutive model for SA508−Ⅲ steel: modeling and experimental verification, *Mater. Sci. Eng. A*, 634(2015), p. 103.

[27] Y. Han, H. Wu, W. Zhang, D.N. Zou, G.W. Liu, and G.J. Qiao, Constitutive equation and dynamic recrystallization behavior of as-cast 254SMO super-austenitic stainless steel, *Mater. Des.*, 69(2015), p. 230.

[28] Y.V.R.K. Prasad, K.P. Rao, and S. Sasidhara, *Hot Working Guide: a Compendium of Processing Maps*, ASM, Ohio, 1997.

[29] M. Sarebanzadeh, R. Mahmudi, and R. Roumina, Constitutive analysis and processing map of an extruded Mg−3Gd−1Zn alloy under hot shear deformation, *Mater. Sci. Eng. A*, 637(2015), p. 155.

[30] Y.S. Wu, M.C. Zhang, X.S. Xie, J.X. Dong, F.S. Lin, and S.Q. Zhao, Hot deformation characteristics and processing map analysis of a new designed nickel-based alloy for 700°C A-USC power plant, *J. Alloys Compd.*, 656(2016), p. 119.